PCCP

PAPER

View Article Online
View Journal | View Issue

Check for updates

Cite this: *Phys. Chem. Chem. Phys.*, 2019, **21**, 1207

Symmetry-breaking induced large piezoelectricity in Janus tellurene materials†

Yu Chen, [a] Junyi Liu, [a] Jiabing Yu, [a] Yaguang Guo[ab] and Qiang Sun *[ab]

Received 23rd July 2018,
Accepted 1st November 2018

DOI: 10.1039/c8cp04669g

rsc.li/pccp

Structural symmetry-breaking can lead to novel electronic and piezoelectric properties in two-dimensional (2D) materials. In this paper, we propose a 2D Janus tellurene (Te_2Se) monolayer with asymmetric Se/Te surfaces and its derived multilayer structures. The band structure calculations show that the 2D Janus Te_2Se monolayer is an indirect gap semiconductor, and the intrinsic mirror asymmetry combined with the spin–orbit coupling induces the Rashba spin splitting and the out-of-plane spin polarization. Moreover, the absence of both the inversion symmetry and out-of-plane mirror symmetry, together with flexible mechanical properties, results in large in-plane and out-of-plane piezoelectric coefficients that are valuable in 2D piezoelectric materials. Furthermore, the out-of-plane piezoelectric effects can exist in multilayer structures under different stacking sequences while the in-plane piezoelectric effect can only exist in some specific stacking patterns. The piezoelectric coefficients of the Janus Te_2Se monolayer and multilayers exceed those of many Janus transition metal dichalcogenides and other well-known piezoelectric materials (*e.g.*, α-quartz and wurtzite-AlN). The combination of the SOC-induced spin splitting and large piezoelectricity endows the Janus Te_2Se structures with potential for applications in spintronics, flexible electronics and piezoelectric devices.

Published on 16 November 2018. Downloaded by Peking University on 8/7/2019 9:44:12 AM.

1. Introduction

Piezoelectricity in two-dimensional (2D) nanomaterials has attracted growing interest for potential nanoscale piezoelectric applications such as sensors, actuators, energy converters, and energy sources due to the low-dimensional structures, and superior mechanical and piezoelectric performance.[1] Because a piezoelectric material must be non-centrosymmetric, 2D systems without inversion symmetry are hotly pursued for piezoelectricity. A typical example is monolayer MoS_2 in the 2H phase that was proved to possess piezoelectricity in both theory[2] and experiments[3,4] due to the inversion asymmetry, but the small piezoelectric coefficient limits the conversion rate of mechanical–electrical energy thus hindering its practical applications. Compared with the monolayer MoS_2, 2D Janus structures[5–7] can directly break the inversion symmetry and out-of-plane mirror symmetry, showing dramatic structural anisotropy and leading to large in-plane piezoelectricity and additional out-of-plane piezoelectricity. Recent experimental advances reported the synthesis of Janus transition metal dichalcogenide monolayers (MoSSe) based on either MoS_2 or $MoSe_2$ monolayers.[5,6] Furthermore, the experiments also proved the existence of vertical dipoles[5] in the Janus MoSSe monolayer, indicating an intrinsic vertical piezoelectric response. Shenoy *et al.*[7] theoretically reported that the Janus transition metal dichalcogenides (MXY) possess large in-plane and out-of-plane piezoelectric polarizations. In addition, the Janus group-III chalcogenide monolayers[8] were also reported to have superior piezoelectric polarizations.

In non-centrosymmetric 2D materials, on the other hand, spin–orbit coupling (SOC) lifts the degenerate spins at high symmetric *k*-points due to relativistic effects. The mirror asymmetry induced vertical potential gradient further shifts the oppositely momentum-dependent in-plane spin polarizations, leading to Rashba spin splitting,[9] which is promising for spin-based applications. The valley polarizations in 2D monolayer MoS_2 exist due to the inversion asymmetry together with the SOC, making it an ideal candidate material in valleytronics,[10–12] but no Rashba spin splitting exists due to the mirror symmetry. Whereas, the Janus MXY monolayers were reported to induce considerable Rashba spin splitting due to the large SOC effect of heavy transition metals.[13–15] These results reveal the great potential for utilizing these Janus structures in piezoelectric and spintronic device applications. However, so far, the studies of 2D Janus materials are still limited and they were only reported in the structures originally without inversion symmetry. Therefore, a question arises: is it possible to modify the intrinsic centrosymmetric 2D materials to form Janus structures for piezoelectric and spintronics applications?

[a] *Department of Materials Science and Engineering, Peking University, Beijing 100871, China. E-mail: sunqiang@pku.edu.cn*
[b] *Center for Applied Physics and Technology, Peking University, Beijing 100871, China*

† Electronic supplementary information (ESI) available. See DOI: 10.1039/c8cp04669g

Published on 16 November 2018. Downloaded by Peking University on 8/7/2019 9:44:12 AM.

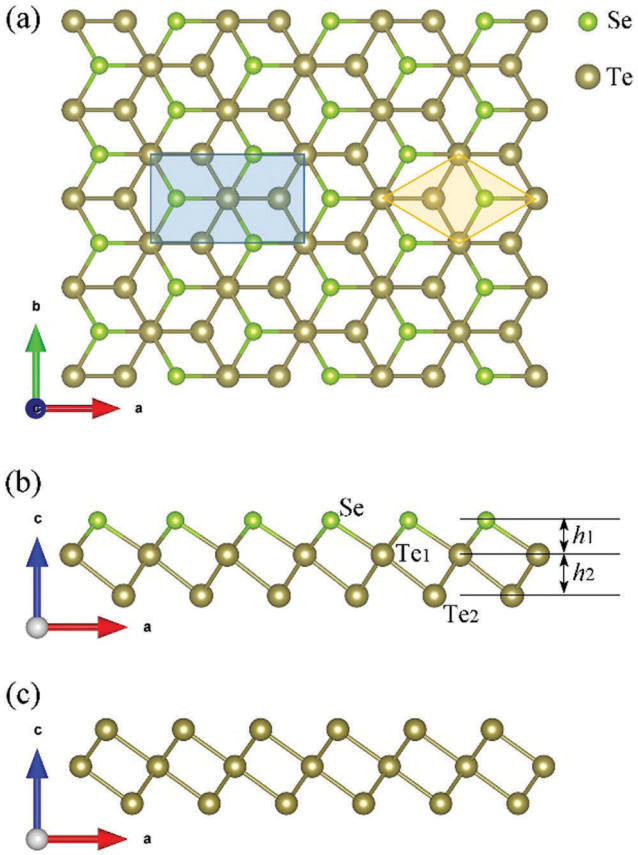

Fig. 1 Atomic structures of the (a) top view and (b) side view of the two-dimensional Janus Te_2Se monolayer. The unit cell is marked with an orange rhombus and the rectangular cell is marked with a blue box for the DFT piezoelectric coefficient calculations. The dark green and bright green balls represent Te and Se atoms, respectively. h_1 and h_2 are the interval distances between the upper Se layer and central Te layer and between the lower Te layer and central Te layer. (c) Atomic structure of the side view of the pristine 2D tellurene monolayer.

Very recently, tellurium-based 2D monolayers (tellurene), a new class of monoelemental 2D atomic crystal materials, have been proposed to possess intriguing geometric structures and physical properties.[16,17] Among the three phases of 2D tellurene (α-, β-, and γ-Te), α-tellurene (see Fig. 1c) is the most stable structure in the tellurium-based monolayer, which is equivalent to the 1T phase of 2D transition-metal dichalcogenide materials (MX_2), where M is a transition metal atom and X is a chalcogen atom including tellurium. α-tellurene was found to be a nearly direct bandgap semiconductor with high carrier mobilities, indicating potential applications in electronic devices. However, it displays intrinsic inversion symmetry, thus there is no piezoelectricity and spin splitting in this structure. In this work, we design the centrosymmetry-breaking structure of 2D Janus tellurene structures (Janus Te_2Se) by replacing Te atoms in the top layer of the pristine α-tellurene with Se atoms, considering the chemical similarity between Te and Se atoms and the experimental feasibility. As shown in Fig. 1a and b, the introduction of Se atoms in the Janus Te_2Se monolayer breaks the inversion symmetry and the SOC induced in-plane Rashba spin splitting and out-of-plane spin polarization are found in the electronic structures. The considerable piezoelectric polarization combined with the more flexible mechanical property induces large in-plane piezoelectricity. Furthermore, the absence of mirror symmetry results in an out-of-plane piezoelectric coefficient, which is highly desired in 2D piezoelectric materials for increasing the degree of freedom of piezoelectric devices. In the multilayer derived structures, the in-plane piezoelectric effect exists in the structures with specific orientations between adjacent monolayers, while the large out-of-plane piezoelectric effects always exist regardless of the stacking sequences. Our calculations show that the Janus Te_2Se materials with large piezoelectricity and spin splitting characters are promising candidates for piezoelectric and spintronic applications.

2. Computational methods

2.1 Computation details

Our calculations are based on density functional theory (DFT) using the VASP package.[18] The interaction between electrons and nuclei is treated using the projected augmented wave (PAW) method[19] with a kinetic cutoff energy of 520 eV. The exchange–correlation functional within the generalized gradient approximation (GGA) framework is taken into account using the Perdew–Burke–Ernzerhof (PBE) form.[20] To achieve better accuracy of the electronic properties, the hybrid Heyd–Scuseria–Ernzerhof (HSE06) functional[21] is further used. Bader charge analysis[22] is performed using the code[23–25] developed by Henkelman's group to estimate the total electronic charge of atoms. For the Janus Te_2Se monolayer, a vacuum spacing of 15 Å along the z direction is included to avoid interactions between two neighboring images. For the Janus Te_2Se multilayers, the van der Waals interactions are treated using the optB88-vdw functional.[26–29] The reciprocal space of the Janus Te_2Se monolayer and multilayers is sampled using the $(15 \times 15 \times 1)$ and $(15 \times 15 \times 5)$ grid meshes and the Monkhorst–Pack special k-point scheme,[30] respectively. The criteria of total energy and Hellmann–Feynman force are 1×10^{-6} eV and 1×10^{-3} eV Å^{-1}, respectively. All the structures are fully relaxed using the conjugated gradient scheme without any symmetry constraints. The phonon dispersions are performed using a finite difference approach as implemented in the Phonopy package.[31]

2.2 Calculation of piezoelectricity

The piezoelectric tensors and piezoelectric strain tensors are defined as

$$e_{ijk} = \frac{\partial P_i}{\partial \varepsilon_{jk}} = e_{ijk}^{\mathrm{elc}} + e_{ijk}^{\mathrm{ion}} \quad (1)$$

and

$$d_{ijk} = \frac{\partial P_i}{\partial \sigma_{jk}} = d_{ijk}^{\mathrm{elc}} + d_{ijk}^{\mathrm{ion}} \quad (2)$$

where P_i, ε_{jk}, and σ_{jk} are the piezoelectric polarizations, strains, and stresses, respectively. The subscripts (i, j, and k) = (1, 2, and 3)

 This journal is © the Owner Societies 2019

Published on 16 November 2018. Downloaded by Peking University on 8/7/2019 9:44:12 AM.

represent the *x*-, *y*-, and *z*-directions, respectively. The first term e_{ijk}^{elc} (d_{ijk}^{elc}) of the left side in eqn (1) and (2) is the clamped-ion piezoelectric tensors resulting from the pure electronic contribution with the fixed ionic positions. In contrast, the relaxed-ion piezoelectric tensors e_{ijk}(d_{ijk}) are obtained from the sum of ionic and electronic contributions with the fully relaxed ionic positions. The relaxed-ion coefficients would be more reliable because they are experimentally relevant.[2,4] Employing the Voigt notation, the piezoelectric tensors e_{ij} can be written as

$$e_{ij} = \begin{Bmatrix} e_{11} & e_{12} & \cdots & e_{16} \\ e_{21} & e_{22} & \cdots & e_{26} \\ e_{31} & e_{32} & \cdots & e_{36} \end{Bmatrix} \quad (3)$$

where the subscripts $i(j)$ = (1, 2,..., 6). The symmetry of the structure will further reduce the number of independent tensor coefficients.

For the 2D Janus Te_2Se monolayer, the introduction of a Se atom breaks the inversion symmetry of the pristine structure, resulting in a lower degree of C_{3v} symmetry. Together with the absence of the inversion symmetry, both the in-plane and out-of-plane piezoelectric effects are allowed in the Janus Te_2Se monolayer when a uniaxial in-plane biaxial strain is applied. Combining the relation between e_{ik} and d_{ij}

$$e_{ik} = d_{ij}C_{jk} \quad (4)$$

The piezoelectric tensors of this 2D structure can be written as[7]

$$e_{ik} = \begin{Bmatrix} e_{11} & -e_{11} & 0 \\ 0 & 0 & -e_{11}/2 \\ e_{31} & e_{31} & 0 \end{Bmatrix} \quad (5)$$

$$d_{ij} = \begin{Bmatrix} d_{11} & -d_{11} & 0 \\ 0 & 0 & -d_{11} \\ d_{31} & d_{31} & 0 \end{Bmatrix} \quad (6)$$

Here, the piezoelectric tensor coefficients of e_{11} and e_{31} are nonzero, while the piezoelectric tensor coefficients are zero for the *y*-direction because this structure is symmetric along this direction (see Fig. 1a). Calculating the values of e_{11} and e_{31}, the corresponding piezoelectric strain tensor coefficients of d_{11} and d_{31} are found to be

$$d_{11} = e_{11}/(C_{11} - C_{12}) \quad (7)$$

and

$$d_{31} = e_{31}/(C_{11} + C_{12}) \quad (8)$$

For the Janus Te_2Se multilayers, the piezoelectric tensors can be expressed as

$$e_{ik} = \begin{Bmatrix} e_{11} & -e_{11} & 0 & 0 & e_{15} & 0 \\ 0 & 0 & 0 & e_{15} & 0 & -e_{11}/2 \\ e_{31} & e_{31} & e_{33} & 0 & 0 & 0 \end{Bmatrix} \quad (9)$$

$$d_{ij} = \begin{Bmatrix} d_{11} & -d_{11} & 0 & 0 & d_{15} & 0 \\ 0 & 0 & 0 & d_{15} & 0 & -2d_{11} \\ d_{31} & d_{31} & d_{33} & 0 & 0 & 0 \end{Bmatrix} \quad (10)$$

In these three-dimensional structures, the piezoelectric tensor coefficients of e_{11}, e_{15}, e_{31}, and e_{33} are nonzero. Using the relation of eqn (4), the three piezoelectric strain coefficients can be written as

$$d_{11} = e_{11}/(C_{11} - C_{12}) \quad (11)$$

$$d_{31} = (C_{33}e_{31} - C_{13}e_{33})/[(C_{11} + C_{12})C_{33} - 2C_{13}^2] \quad (12)$$

$$d_{33} = ((C_{11} + C_{12})e_{33} - 2C_{13}e_{31})/[(C_{11} + C_{12})C_{33} - 2C_{13}^2] \quad (13)$$

To obtain the piezoelectric properties of the Janus Te_2Se monolayer and multilayers, the elastic stiffness tensor, c_{ij}, and piezoelectric tensor, e_{ijk}, are calculated by using the finite difference method and density functional perturbation theory (DFPT) method as implemented in the VASP package, respectively, which have been reported in many works.[32–35] To accurately calculate these tensor components, the highly dense *k*-point meshes, ($25 \times 25 \times 1$) and ($25 \times 25 \times 9$), are used for monolayer and multilayers, respectively. A large vacuum spacing of about 30 Å is used for this buckled 2D hexagonal structure of the Janus Te_2Se to converge the piezoelectric coefficients due to the large electrostatic interactions. The accuracy of our computations is tested by calculating the piezoelectric coefficients of the monolayer MoS_2 using the above methods, and the computed results ($d_{11[clamped\text{-}ion]} = 2.850$ pm V^{-1}; $d_{11[relaxed\text{-}ion]} = 3.672$ pm V^{-1}) are in good agreement with the previous DFT studies,[2] confirming the validity of our method.

3. Results and discussion

3.1 The geometric structures of the 2D Janus Te_2Se monolayer

The geometric structures of the Janus Te_2Se monolayer are shown in Fig. 1a and b, which consist of of three atomic layers of Se, Te, and Te from top to bottom with the unconventional asymmetric construction. After optimization, the Janus Te_2Se monolayer conserves the tri-layered hexagonal structure with C_{3v} symmetry. The structural feature of the Janus Te_2Se monolayer can be associated with the unique chemical character of a Te atom, which has the dual characteristics of both metal and nonmetal. Similar to the tellurene monolayer,[16] the central Te atoms are more metallic with a large coordination number, while both the outer Te and Se atoms are more semiconducting with a smaller coordination number. Thus, the central Te atom in the Janus Te_2Se monolayer can act as a metal in analogy with the metallic Mo atom of 2D MoS_2 in the 1T-phase. The lattice constant of the Janus Te_2Se monolayer is a = 4.108 Å, and the interval distance between the upper Se layer and the lower Te layer is $h_1 + h_2$ = 3.457 Å (h_1 = 1.578 Å, h_2 = 1.879 Å), which are shorter than the tellurene monolayer (see Fig. 1c) because the smaller Se atoms replace Te atoms in one outer layer. The difference in atomic sizes and electronegativities of Te and Se

Published on 16 November 2018. Downloaded by Peking University on 8/7/2019 9:44:12 AM.

atoms leads to inequivalent Te–Te and Te–Se bond lengths and bond characteristics. The Te–Te bond length is d_1 = 3.026 Å, which is in agreement with the previous report,[16] while the Te–Se bond length is found to be d_2 = 2.849 Å.

3.2 Stability

To study the stability of the 2D Janus Te_2Se monolayer, we first calculate the phonon dispersion with a $(7 \times 7 \times 1)$ supercell to validate its dynamic stability. Non-analytical term correction is adopted to include dipole–dipole interaction.[36,37] As shown in Fig. 2a, there is no imaginary vibrational frequency in the first Brillouin zone, moreover, just like most 2D materials,[38,39] both linear and flexural modes occur around the Gamma point, which clearly suggests that the 2D Janus Te_2Se monolayer is dynamically stable. To further exam its thermal stability at finite-temperature, we perform *ab initio* molecular dynamics (AIMD) simulation by using the canonical (*NVT*) ensemble. A $(6 \times 6 \times 1)$ supercell is used for the 2D Janus structure to minimize the constraint induced by periodicity. The simulations are carried out using a Nosé thermostat at 300 K for 9 ps with a time step of 1 fs. As shown in Fig. 2b, the total energy fluctuates in the simulation time but the average energy remains almost invariant. From the final atomic configuration of the 2D Janus structure in Fig. 2b, we can find no obvious distortion of the geometric structure after 9000 steps of AIMD simulation and optimizing this final configuration can allow returning to its initiating structure. These results indicate that the 2D Janus Te_2Se monolayer is thermally stable at room temperature.

Additionally, considering the experimental facts that the Janus MoSSe monolayers were synthesized either by replacing the top-layer S with Se atoms on the 2D MoS_2 monolayer or by controlled sulfurization of the 2D $MoSe_2$ monolayer,[5,6] we further study the thermodynamic stability of the 2D Janus Te_2Se monolayer by calculating the formation energy (ΔH) based on the hypothetical reaction equation written as: $Te_{2D} + Se_{3D} \rightarrow Te_2Se_{Janus}$. Hence, the formation energy (ΔH) becomes

$$\Delta H = (n_1 \times E_{Janus} - n_2 \times E_{Te[2D]} - n_3 \times E_{Se[3D]})/n_1, \quad (14)$$

where E_{Janus} is the energy (eV per atom) of the Janus Te_2Se monolayer; $E_{Te[2D]}$ and $E_{Se[3D]}$ are the energies (eV per atom) of the 2D tellurene monolayer and selenium bulk phase, respectively; and n_1 and n_2 (n_3) are the total number of atoms and the number of atoms of Te (Se) in a unit cell. Thus the formation energy of the Janus Te_2Se monolayer is ΔH_{Janus} = −0.021 eV per atom. For comparison, we also calculate the formation energy of $SeTe_2$ in the symmetrical structure where the Se atom is in the middle layer and the two Te atoms are in the top and bottom layers. The value of ΔH_{sys} is 0.158 eV per atom, which is positive and higher than that of Janus Te_2Se. Therefore, the Janus Te_2Se monolayer is energetically favorable.

3.3 Electronic properties

The electronic structures of the 2D Janus Te_2Se monolayer are plotted in Fig. 3b. Due to the similarity in the structure of the Janus Te_2Se monolayer with 2D α-tellurene,[16] the band structure of the 2D Janus structure is also very similar to that of tellurene. The Janus Te_2Se monolayer is found to be a semiconductor with an indirect band gap of E_g = 0.72 eV at the PBE level (green lines in Fig. 3b), and the highest valence band (HVB) and lowest conduction band (LCB) are located at the low-symmetric *k*-point (K') and the Γ point in the first Brillouin zone, respectively. Since the PBE-functional calculations will significantly underestimate the band gap, we also calculate the band structure using the screened hybrid HSE06 functional to better describe the exchange-correction energy of electrons. As shown in Fig. 3b (gray lines), both the PBE and HSE06 functionals give rise to similar energy band dispersions of the valence and conduction bands, while the valence bands are downshifted at the HSE06 level, resulting in a larger band gap of E_g = 1.07 eV for the 2D Janus Te_2Se monolayer. These values are comparable to that of 2D tellurene using the same functional. By projecting the density of states onto different atoms (PDOS), we find that the HVB is mainly contributed by the p-orbitals of the upper Se and lower Te atoms, while the LCB is dominated by the p-orbitals of the two Te atoms in the unit cell with minor contributions from the Se-p orbitals.

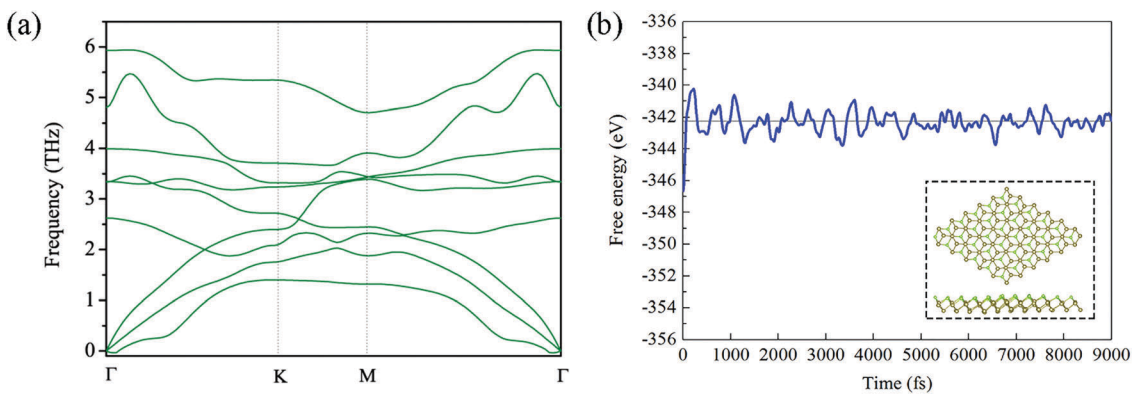

Fig. 2 (a) The calculated phonon spectra of the 2D Janus Te_2Se monolayer along the high symmetric *k*-point path in the first Brillouin zone. The high symmetry *k* points: Γ (0, 0, 0), *K* (−1/3, 2/3, 0), and *M* (0, 1/2, 0). (b) Energy fluctuation of the 2D Janus Te_2Se monolayer with respect to time in AIMD simulation at 300 K. The inset shows the snapshot of the final geometry depicting structural change in the 2D Janus Te_2Se monolayer in the AIMD simulation at 300 K.

 This journal is © the Owner Societies 2019

Published on 16 November 2018. Downloaded by Peking University on 8/7/2019 9:44:12 AM.

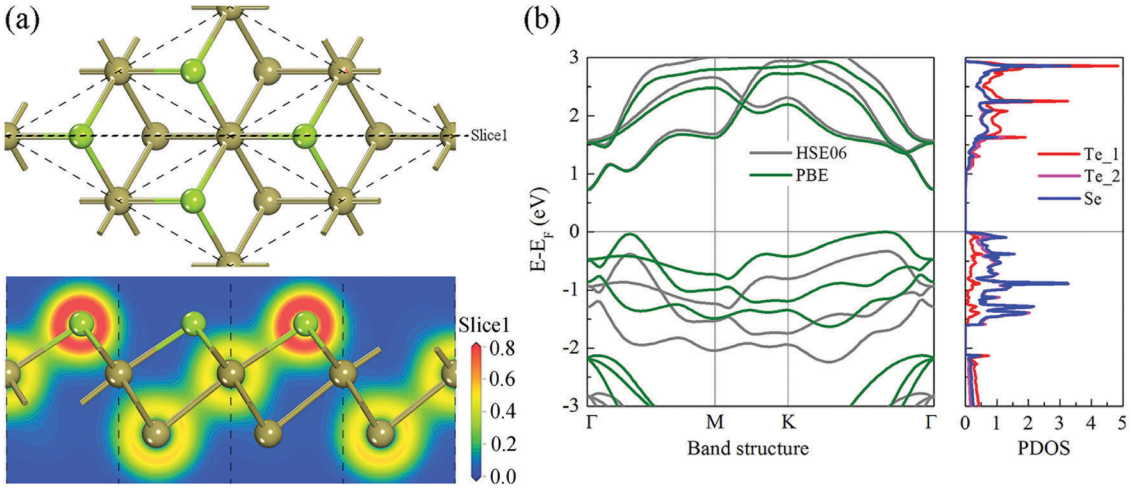

Fig. 3 (a) The total charge density of the 2D Janus Te_2Se monolayer is plotted at the horizontal and vertical cross sections indicated by the black dashed line. (b) The band structures and corresponding partial DOS of the 2D Janus Te_2Se monolayer with green and gray lines representing the results using PBE and HSE06 functionals, respectively.

The planar average of the electrostatic potential energy is plotted in Fig. 4a. We can see that the mirror asymmetry results in an electrostatic potential gradient ($\Delta\phi$) of about 0.5 eV, which is related to the work function change of the structure.[15] Due to the electron redistribution in the Janus monolayer structure, the local electric fields between central Te (Te_1) and outer Te (Te_2), and between Te_1 and Se are formed with the directions indicated by the olive and green arrows. Consequently, there is the net electric field from Te_2 to Se represented by the red arrow. The magnitude of the inherent electric field is 2.006 eV Å^{-1}, as determined by the slope of the plane-averaged electrostatic potential between two outermost atom minima (see the red dashed line in Fig. 4a). This value is larger than that of Janus MoSSe (0.856 eV Å^{-1}), implying a stronger vertical polarization in the Te_2Se monolayer. The total charge density plotted in Fig. 3a shows the charge distributions of the Janus Te_2Se monolayer. One can see that more charges are transferred from Te_1 to Se than to Te_2, which can be further confirmed by the Bader charge analysis. The charge transfers from the central Te atoms to the outer Se and Te atoms are about 0.42 e and 0.19 e, respectively, therefore, the charge transfer difference leads to the net electric field from the outer Te to Se.

More importantly, the absence of vertical mirror symmetry combined with the SOC effect in the 2D materials brings out Rashba-like and Zeeman-like band splitting.[40] We plot the band structure of the 2D Janus Te_2Se monolayer with the SOC included in Fig. 4b–d. One can observe that the inclusion of SOC removes the spin degeneracy and both the LCBs and HVBs experience obvious band splitting. Interestingly, there is valley spin splitting in the HVBs at the low-symmetric K' point due to the existence of the net electric dipole moment of the system, and the band splitting parameter of λ_V (see Fig. 4d) is about 24 meV. Moreover, the mirror asymmetry facilitates Rashba spin splitting (see Fig. 4c) in the LCBs at the high-symmetric Γ point,

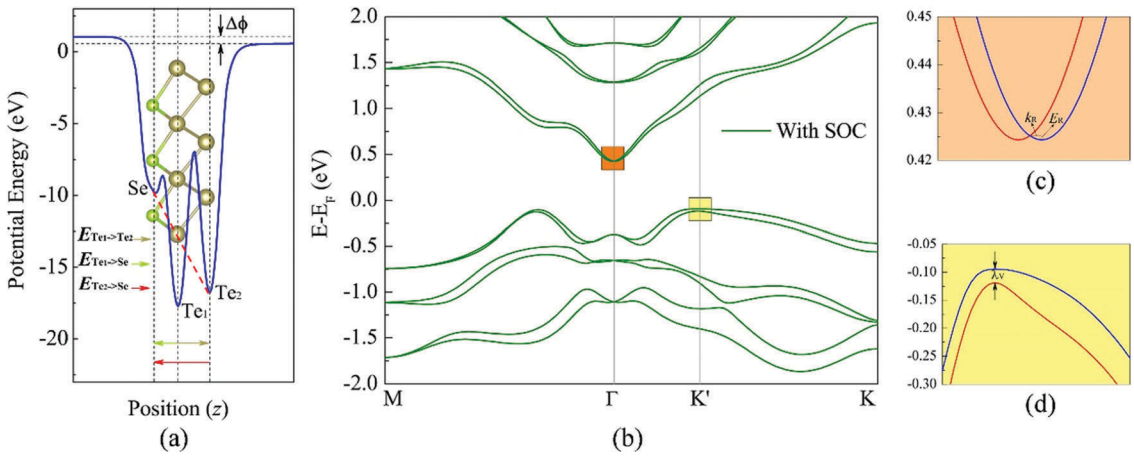

Fig. 4 (a) Planar average of the electrostatic potential energy of the 2D Janus Te_2Se monolayer. The arrows indicate the direction of the local electric fields. (b) The band structure with the spin–orbit coupling (SOC) of the 2D Janus Te_2Se monolayer. (c) and (d) The amplified band structures of the lowest conduction bands around the Γ point and the highest valence bands around the K' point.

Published on 16 November 2018. Downloaded by Peking University on 8/7/2019 9:44:12 AM.

which means that the shift of energy bands in the momentum space leads to in-plane spin polarization. To understand the origin of band splitting in the 2D Janus Te_2Se monolayer, we plot the atom-projected and orbital-projected band structures in Fig. 5. Seen from the orbital character distributions, we find that the HVBs at the low-symmetric K' point show a predominant weight from the in-plane $p_x + p_y$ orbitals of the outer Te and Se atoms, while the LCBs at the Γ point present a strong weight of the out-of-plane p_z orbitals of Te atoms. Therefore, we think that the Te-p_z orbital mainly contributes to Rashba spin splitting. For the C_{3v} symmetric 2D system, the spin splitting Hamiltonian[14,40] can be described as $H(k) = v_k(k_x\sigma_y - k_y\sigma_x) + \lambda_k(3k_x^2 - k_y^2)k_y\sigma_z$, where $v_k = (1 + \alpha k^2)$ and $k = \sqrt{k_x^2 + k_y^2}$; σ_i, λ_i, and α are the Pauli matrices, warping parameter, and Rashba parameter, respectively. The first term induces the in-plane Rashba band splitting in the LCBs at the Γ point, while the second term causes the out-of-plane band splitting in the HVBs at the K' point. Using the linear Rashba model, the SOC-induced band splitting is characterized by the so-called Rashba parameter (α_R)[13] as $\alpha_R = \frac{2E_R}{k_R}$, where E_R and k_R are the Rashba energy splitting and the momentum shift, respectively, as marked in Fig. 4c. The parameters of E_R and k_R are 0.92 meV and 0.0047 Å^{-1}, respectively, thus α_R is calculated to be 0.39 eV Å for the LCBs at the Γ point. Although this value is much smaller than that previously reported in the BiTeI monolayer[41] or $LaOBiS_2$ film[42] due to the fact that the strength of the SOC in the p orbitals of the chalcogenide atoms is much weaker than that in other heavy metallic elements, it is still comparable to the Janus MoSSe monolayer[14] and GaSe/$MoSe_2$ heterostructures,[43] indicating potential applications in spintronic devices.

3.4 Piezoelectricity of the Janus Te_2Se monolayer

To study the piezoelectricity of the Janus Te_2Se monolayer, we first calculate the elastic stiffness coefficients of C_{11} and C_{12} ($C_{11} = C_{22}$ for this hexagonal lattice) and the non-zero piezoelectric tensors of e_{11} and e_{31}. The so-called relaxed-ion and clamped-ion elastic stiffness coefficients of the Janus monolayer are listed in Table 1 and Table S1 (see the ESI†). The monolayer has relaxed-ion constants of C_{11} = 38.8 N m^{-1} and C_{12} = 10.5 N m^{-1}, on the other hand, the clamped-ion components give larger values of C_{11} = 57.9 N m^{-1} and C_{12} = 15.2 N m^{-1}. We notice that these values are comparable to those of the pristine tellurene monolayer calculated by the same methods, but they are obviously smaller than those of other structures[2,7,8] listed in Table 1, indicating that the 2D Janus Te_2Se monolayer is more flexible than other 2D materials. The less-stiff mechanical properties of the 2D Janus Te_2Se monolayer originate from its intrinsic electronic properties. In the 2D Janus structure, the covalent bonding is much weaker than in other 2D materials, which can be reflected in the bond lengths that are longer than those of the Te bulk material[44] (d = 2.86 Å), the Se bulk material[45] (d = 2.30 Å), and 2D $MoTe_2$ monolayer[46] (d = 2.73 Å).

Then we calculate the piezoelectric coefficients of the 2D Janus Te_2Se monolayer. According to eqn (7) and (8), the values of d_{11} and d_{31} can be calculated with the piezoelectric coefficients e_{11} and e_{31}, and the elastic coefficients C_{11} and C_{12}. The values of the piezoelectric coefficients e_{11} and e_{31} (d_{11} and d_{31}) of the 2D Janus Te_2Se monolayer are listed in Table 1 and Table S1 (ESI†). One can see that the relaxed-ion piezoelectric coefficient of e_{11} is larger than the clamped-ion one and is also slightly larger than those of other three 2D materials. However, the relaxed-ion piezoelectric strain coefficient of d_{11}, which depicts the conversion ratio between the mechanical energy and electrical energy, shows a much larger value than other 2D materials. This is understandable since the 2D Janus Te_2Se monolayer is distinctly softer than other materials, therefore the piezoelectric strain coefficient of d_{11} highly relies on the mechanical properties of the structure. The elastic constants (C_{11} and C_{12}) clearly indicate that the large piezoelectric effect is

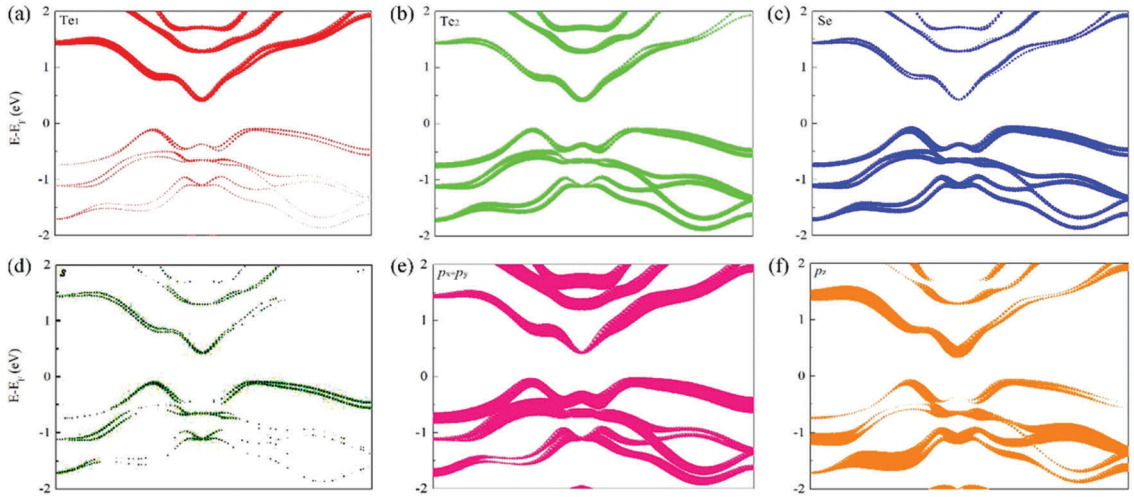

Fig. 5 Band structures with the SOC projected on the atoms: (a) Te_1, (b) Te_2, (c) Se, and orbitals: (d) s, (e) $p_x + p_y$, (f) p_z of the 2D Janus Te_2Se monolayers. The radius of the circles represents the weight of each atom and orbital.

 This journal is © the Owner Societies 2019

Published on 16 November 2018. Downloaded by Peking University on 8/7/2019 9:44:12 AM.

Table 1 The relaxed-ion elastic stiffness constants (C_{ij}) and piezoelectric coefficients (e_{ij}/d_{ij}) of the 2D Janus Te_2Se monolayer. The corresponding coefficients of the 2D tellurene, MoS_2, the Janus MoSTe, and the Janus In_2SSe monolayers are listed for comparison as well. The units of C_{ij}, e_{ij}, and d_{ij} for these 2D materials are N m^{-1}, 10^{-10} C m^{-1}, and pm V^{-1}, respectively

Materials	C_{11}	C_{12}	e_{11}	e_{31}	d_{11}	d_{31}
Janus Te_2Se	38.82	10.49	4.614	0.123	16.285	0.249
α-Tellurene	34.2	9.8	—	—	—	—
MoS_2[2]	130	32	3.64	—	3.73	—
Janus MoSTe[7]	112.7	22.7	4.53	0.038	5.036	0.028
Janus In_2SSe[8]	55	17	3.24	0.13	8.47	0.18

attributed to the mechanical responses. The relaxed-ion value of d_{11} is calculated to be as large as 16.28 pm V^{-1}, which is much higher than that of the widely used bulk materials like α-quartz (d_{11} = 2.3 pm V^{-1}) and wurtzite-AlN (d_{33} = 5.4 pm V^{-1}),[47,48] suggesting that the 2D Janus Te_2Se monolayer may have large in-plane piezoelectric effects when being applied with a uniaxial strain.

On the other hand, we should note that there are a limited number of 2D materials[5,12,13] that have been reported to have out-of-plane piezoelectric effects. Therefore, it is interesting to see that the 2D Janus Te_2Se monolayer possesses the out-of-plane piezoelectric coefficients of e_{31} (d_{31}) due to the mirror asymmetry, which means that applying an in-plane uniaxial strain can also induce the out-of-plane piezoelectric effect. The value of d_{31} = 0.25 pm V^{-1} is smaller by two orders of magnitude compared to the in-plane coefficient d_{11}, but it is still comparable to that of the 2D Janus MXY monolayers[7] and the 2D Janus In_2SSe monolayer.[8] Thus, we should expect that the 2D Janus Te_2Se monolayer with flexible mechanical properties, large in-plane piezoelectricity and desired out-of-plane piezoelectric effect would show a higher degree of flexibility in potential piezoelectric applications.

3.5 Piezoelectricity of the Janus Te_2Se multilayers

On the other hand, one of the most promising applications of 2D materials is the controllable vertical stacking of the functional 2D layers as seen in 2D multilayer van der Waals heterostructures, which show a wide range of possible applications in electronic, optoelectronic, energy storage and catalysis.[49] In experiments, 2D layered materials can be transferred from the substrate to other layer surfaces using mechanical exfoliation methods or heterostructures are synthesized by van der Waals epitaxy on top of 2D materials. Since we have demonstrated promising in-plane and out-of-plane piezoelectric effects in the 2D Janus Te_2Se monolayer, we further consider the piezoelectric properties of the Janus Te_2Se multilayer structures that are constructed by stacking Janus monolayers with different stacking orientations and sequences. Five possible structures are plotted in Fig. 6, where the outer Se atoms are always above the central Te atoms, while the outer Te atoms are underneath the central Te atoms, ensuring that the out-of-plane piezoelectricity will not be counteracted due to the vertical flipping of one of the layers in the unit cells. The lattice parameters and relative energy of the five structures are listed in Table S2 (ESI†). We find that the multilayer structure with parallel A–A stacking (see Fig. 6a) is the most stable structure with the lowest energy among the five structures and the energy differences of the five unit-cells are within about 52 meV per atom. To confirm the dynamic stability of the Janus Te_2Se multilayers, we take the first multilayer structure in Fig. 6a as an example to calculate the phonon spectra. As shown in Fig. S1 in the ESI,† the phonon dispersions without imaginary frequency indicate the dynamic stability of the Janus Te_2Se multilayers. The lattice parameter of a lies in the 4.091 to 4.157 Å range, which is related to that of the 2D Janus Te_2Se monolayer (a = 4.108 Å), while the lattice parameter c shows a wide range from 12.115 to 14.267 Å due to the different stacking configurations and overlaps between the Se atoms in the lower layer and the Te atoms in the upper layer along the z-direction in the unit cells. It is interesting to see that the parameter of c increases with decreasing parameter a, leading to the increase of the corresponding unit-cell volume of V, which is inversely correlated with the energy of these Janus multilayer structures.

The relaxed-ion and clamped-ion elastic constants of the Janus multilayers are reported in Table 2 and Table S3 in the ESI,†

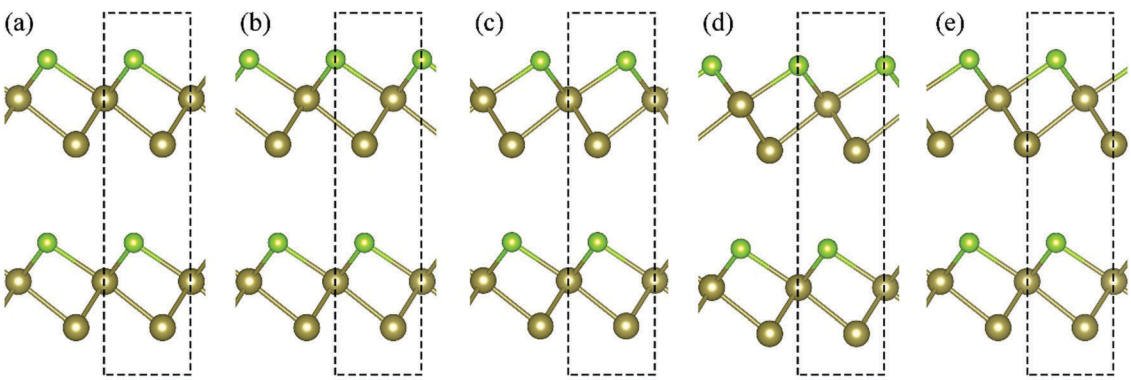

Fig. 6 The Janus Te_2Se multilayer structures with five high-symmetry stacking sequences. The unit cells with lattice parameters a and c are marked in the dashed lines. The two Janus layers in the unit cells of (a) and (b) have parallel orientations in the basal plane, and those in (c)–(e) have antiparallel orientations.

Published on 16 November 2018. Downloaded by Peking University on 8/7/2019 9:44:12 AM.

Table 2 The relaxed-ion elastic constants (C_{ij}) and the relaxed-ion piezoelectric coefficients (e_{ij}/d_{ij}) of the unit cell of Janus Te_2Se multilayers with the structures shown in Fig. 6. The units of C_{ij}, e_{ij} and d_{ij} for these multilayer structures are GPa, 10^{-10} C m^{-1} and pm V^{-1}, respectively

Structure	C_{11}	C_{12}	C_{13}	C_{33}	e_{11}	e_{31}	e_{33}	d_{11}	d_{31}	d_{33}
(a)	69.70	17.68	18.57	23.68	1.749	−0.270	−1.524	33.627	15.902	−89.338
(b)	56.22	20.82	11.86	34.03	0.774	−0.053	−0.372	21.865	1.122	−11.725
(c)	57.86	18.36	11.00	35.60	0	−0.016	−0.388	0	1.501	−11.812
(d)	60.08	25.72	19.80	32.19	0	−0.112	−0.503	0	3.213	−19.595
(e)	57.49	23.65	13.89	26.36	0	−0.262	−0.953	0	3.614	−39.947

which are also significantly smaller than those of the bulk MoS_2 or the Janus MXY multilayers.[7] Then we calculate the piezoelectric coefficients of the Janus Te_2Se multilayers using eqn (11)–(13). We first observe that for the structures in Fig. 6c–e, the in-plane piezoelectricity coefficients of e_{11} and d_{11} are zero, implying that these multilayer structures may not have in-plane piezoelectric effects. Similar to the previous report of the Janus transition metal dichalcogenide multilayers,[7] in these three stacking configurations, the two Janus layers in a unit cell have anti-parallel orientations in the basal plane. Therefore, the in-plane piezoelectric effect generated by one layer in a unit cell will be opposite to that generated by another layer, so the two effects will cancel out each other, resulting in no in-plane piezoelectricity in these multilayer structures. While for multilayer structures in Fig. 6a and b, the two monolayers have parallel orientations in the basal plane, thus the two structures possess in-plane piezoelectricity. In particular the clamped-ion coefficients (d_{11}) of the Janus Te_2Se multilayers (Fig. 6a and b) are about 11.56 and 10.25 pm V^{-1} (see Table S1, ESI†), that are close to the value of 9.38 pm V^{-1} for the Janus Te_2Se monolayer, while the relaxed-ion values of d_{11} in these two structures show distinct differences. So we deduce that interlayer van der Waals interactions will affect the ion relaxations of the multilayer structures, thus altering the in-plane polarizations of each Janus layer.

The out-of-plane piezoelectric effects exist in all five structures due to no flipping configuration of two Janus layers in the unit cells. The relaxed-ion values of piezoelectric coefficients of e_{31} and e_{33} and the corresponding clamped-ion coefficients are listed in Table 2 and Table S3 (ESI†), respectively. From eqn (11)–(13), we see that the piezoelectric strain coefficients (d_{ij}) are highly coupled to the elastic constants (C_{ij}) and piezoelectric coefficients (e_{ij}). The relaxed-ion piezoelectric coefficients are much greater than the clamped-ion ones, indicating that the ionic contribution to the piezoelectric polarization is larger than the electronic contribution for all the multilayer structures. For the Janus multilayer structures, the magnitude of the piezoelectric strain coefficient of d_{33} is much larger than that of d_{31}, indicating that applying the vertical strains along the z direction to the Janus multilayers can give rise to stronger out-of-plane piezoelectric effects than the in-plane strains. Furthermore, the values of d_{33} vary with different stacking sequences ranging from 11.73 pm V^{-1} to 89.34 pm V^{-1}, demonstrating that the van der Waals interactions also significantly affect the out-of-plane piezoelectric polarizations in the Janus Te_2Se multilayer structures. And the larger lattice parameter of c basically gives smaller relaxed-ion piezoelectric coefficients, which may be due to the fact that the larger lattice parameter of multilayer structures possesses a smoother potential energy surface, thus the internal relaxation will change the total energy in a smaller degree than that in the ones with smaller lattice parameters.[34] From the above calculations, we see that the multilayer structure with a parallel A–A stacking sequence in Fig. 6a has the lowest total energy and the largest piezoelectric coefficients: d_{11} = 33.63 pm V^{-1}, d_{31} = 15.90 pm V^{-1} and d_{33} = 89.34 pm V^{-1}. These values are comparable to that of monolayer group-IV monochalcogenides showing giant piezoelectricity (d_{11} = 75.43–250.58 pm V^{-1}; d_{12} = 22.89–97.17 pm V^{-1}).[50] We note that though we only consider five structures with high-symmetry stacking sequences, the values of piezoelectric coefficients should be sufficient to include other multilayer structures with arbitrary stacking orientations since an arbitrary orientation can be treated as the intermediate state between two high-symmetry stacking sequences in these five multilayer structures. The in-plane piezoelectric coefficient of d_{11} of the Janus Te_2Se multilayer materials changes in the range of 0–33.63 pm V^{-1}, depending on the different orientations in the basal plane where the piezoelectric effects of the two monolayers in the multilayer structure may be partially offset or enhanced by each other. In addition, the out-of-plane coefficient d_{33} of these materials ranges from 11.73 to 89.34 pm V^{-1} hinging on the different van der Waals interactions between adjacent layers. Based on the above discussion and analysis, we can expect that the appreciable in-plane and out-of-plane piezoelectric effects in the Janus Te_2Se multilayers would endow these materials with multiple functions for piezoelectric applications.

4. Conclusions

In summary, we have studied the stability, electronic and piezoelectric properties of the 2D Janus tellurene (Te_2Se) monolayer and its derived multilayers by using first-principles calculations. We find that the 2D Janus Te_2Se monolayer is dynamically, thermally, and energetically stable. The electronic structure calculation shows different charge distributions on the two sides of the 2D Janus monolayer, displaying an indirect bandgap of 1.07 eV. The inversion asymmetry together with the SOC effect induces Rashba-like splitting bands and valley spin polarization at the LCBs and HVBs, respectively. The structural symmetry-breaking and flexible mechanical properties lead to a large in-plane piezoelectric coefficient (d_{11}) of 16.28 pm V^{-1} and an additional out-of-plane piezoelectric coefficient (d_{31}) of 0.24 pm V^{-1} in the 2D Janus Te_2Se monolayer. We also investigate the piezoelectric effects in the Janus Te_2Se multilayer structures and find that

 This journal is © the Owner Societies 2019

Published on 16 November 2018. Downloaded by Peking University on 8/7/2019 9:44:12 AM.

both in-plane and out-of-plane strains can induce strong piezoelectric effects. The Janus Te_2Se multilayer material with the parallel A–A stacking sequence of adjacent Janus layers is found to have the lowest energy and the most outstanding piezoelectric response to external strains. The out-of-plane piezoelectric effects exist in all the multilayer structures and the value of the out-of-plane piezoelectric coefficient d_{33} varies in a wide range from 11.73 to 89.34 pm V^{-1} depending on different stacking sequences. These findings can stimulate experimental interest in exploring the potential spintronic and piezoelectric applications because of the SOC-induced spin splitting and strong piezoelectric effects.

Conflicts of interest

There are no conflicts to declare.

Acknowledgements

This work is partially supported by grants from the National Natural Science Foundation of China (No. NSFC-21573008 and -21773003) and from the Ministry of Science and Technology of China (No. 2017YFA0204902). Calculations are performed on the High Performance Computing Platform of Peking University, China.

References

1 W. Wu and Z. L. Wang, *Nat. Rev. Mater.*, 2016, **1**, 16031.
2 K.-A. N. Duerloo, M. T. Ong and E. J. Reed, *J. Phys. Chem. Lett.*, 2012, **3**, 2871–2876.
3 W. Wu, L. Wang, Y. Li, F. Zhang, L. Lin, S. Niu, D. Chenet, X. Zhang, Y. Hao, T. F. Heinz, J. Hone and Z. L. Wang, *Nature*, 2014, **514**, 470–474.
4 H. Zhu, Y. Wang, J. Xiao, M. Liu, S. Xiong, Z. J. Wong, Z. Ye, Y. Ye, X. Yin and X. Zhang, *Nat. Nanotechnol.*, 2015, **10**, 151–155.
5 A. Y. Lu, H. Zhu, J. Xiao, C. P. Chuu, Y. Han, M. H. Chiu, C. C. Cheng, C. W. Yang, K. H. Wei, Y. Yang, Y. Wang, D. Sokaras, D. Nordlund, P. Yang, D. A. Muller, M. Y. Chou, X. Zhang and L. J. Li, *Nat. Nanotechnol.*, 2017, **12**, 744–749.
6 J. Zhang, S. Jia, I. Kholmanov, L. Dong, D. Er, W. Chen, H. Guo, Z. Jin, V. B. Shenoy, L. Shi and J. Lou, *ACS Nano*, 2017, **11**, 8192–8198.
7 L. Dong, J. Lou and V. B. Shenoy, *ACS Nano*, 2017, **11**, 8242–8248.
8 Y. Guo, S. Zhou, Y. Bai and J. Zhao, *Appl. Phys. Lett.*, 2017, **110**, 163102.
9 Y. A. Bychkov and E. I. Rashba, *JETP Lett.*, 1984, **39**, 78–81.
10 D. Xiao, G. B. Liu, W. Feng, X. Xu and W. Yao, *Phys. Rev. Lett.*, 2012, **108**, 196802.
11 H. Zeng, J. Dai, W. Yao, D. Xiao and X. Cui, *Nat. Nanotechnol.*, 2012, **7**, 490–493.
12 K. F. Mak, K. He, J. Shan and T. F. Heinz, *Nat. Nanotechnol.*, 2012, **7**, 494–498.
13 Y. C. Cheng, Z. Y. Zhu, M. Tahir and U. Schwingenschlögl, *EPL*, 2013, **102**, 57001.
14 F. Li, W. Wei, P. Zhao, B. Huang and Y. Dai, *J. Phys., Lett.*, 2017, **8**, 5959–5965.
15 Q.-F. Yao, J. Cai, W.-Y. Tong, S.-J. Gong, J.-Q. Wang, X. Wan, C.-G. Duan and J. H. Chu, *Phys. Rev. B*, 2017, **95**, 165401.
16 Z. Zhu, X. Cai, S. Yi, J. Chen, Y. Dai, C. Niu, Z. Guo, M. Xie, F. Liu, J. H. Cho, Y. Jia and Z. Zhang, *Phys. Rev. Lett.*, 2017, **119**, 106101.
17 E. J. Reed, *Nature*, 2017, **552**, 40–41.
18 G. Kresse and J. Furthmuller, *Phys. Rev. B: Condens. Matter Mater. Phys.*, 1996, **54**, 11169–11186.
19 G. Kresse and D. Joubert, *Phys. Rev. B: Condens. Matter Mater. Phys.*, 1999, **59**, 1758–1775.
20 J. P. Perdew, K. Burke and M. Ernzerhof, *Phys. Rev. Lett.*, 1996, **77**, 3865–3868.
21 J. Heyd, G. E. Scuseria and M. Ernzerhof, *J. Chem. Phys.*, 2003, **118**, 8207.
22 R. F. W. Bader, *Chem. Rev.*, 1991, **91**, 893–928.
23 G. Henkelman, A. Arnaldsson and H. Jónsson, *Comput. Mater. Sci.*, 2006, **36**, 354–360.
24 E. Sanville, S. D. Kenny, R. Smith and G. Henkelman, *J. Comput. Chem.*, 2007, **28**, 899–908.
25 W. Tang, E. Sanville and G. Henkelman, *J. Phys.: Condens. Matter*, 2009, **21**, 084204.
26 M. Dion, H. Rydberg, E. Schroder, D. C. Langreth and B. I. Lundqvist, *Phys. Rev. Lett.*, 2004, **92**, 246401.
27 G. Roman-Perez and J. M. Soler, *Phys. Rev. Lett.*, 2009, **103**, 096102.
28 J. Klimeš, D. R. Bowler and A. Michaelides, *Phys. Rev. B: Condens. Matter Mater. Phys.*, 2011, **83**, 195131.
29 J. Klimes, D. R. Bowler and A. Michaelides, *J. Phys.: Condens. Matter*, 2010, **22**, 022201.
30 H. J. Monkhorst and J. D. Pack, *Phys. Rev. B: Solid State*, 1976, **13**, 5188–5192.
31 A. Togo, F. Oba and I. Tanaka, *Phys. Rev. B: Condens. Matter Mater. Phys.*, 2008, **78**, 134106.
32 M. M. Alyörük, Y. Aierken, D. Çakır, F. M. Peeters and C. Sevik, *J. Phys. Chem. C*, 2015, **119**, 23231–23237.
33 M. N. Blonsky, H. L. Zhuang, A. K. Singh and R. G. Hennig, *ACS Nano*, 2015, **9**, 9885–9891.
34 C. Sevik, D. Çakır, O. Gülseren and F. M. Peeters, *J. Phys. Chem. C*, 2016, **120**, 13948–13953.
35 M. M. Alyörük, *Phys. Status Solidi B*, 2016, **253**, 2534–2539.
36 R. M. Pick, M. H. Cohen and R. M. Martin, *Phys. Rev. B: Solid State*, 1970, **1**, 910.
37 X. Gonze and C. Lee, *Phys. Rev. B: Condens. Matter Mater. Phys.*, 1997, **55**, 10355.
38 A. Molina-Sanchez, K. Hummer and L. Wirtz, *Surf. Sci. Rep.*, 2015, **70**, 554–586.
39 T. Zhu and E. Ertekin, *Phys. Rev. B: Condens. Matter Mater. Phys.*, 2015, **91**, 205429.
40 H. Yuan, M. S. Bahramy, K. Morimoto, S. Wu, K. Nomura, B.-J. Yang, H. Shimotani, R. Suzuki, M. Toh, C. Kloc, X. Xu, R. Arita, N. Nagaosa and Y. Iwasa, *Nat. Phys.*, 2013, **9**, 563–569.

Published on 16 November 2018. Downloaded by Peking University on 8/7/2019 9:44:12 AM.

41 M. Sakano, M. S. Bahramy, A. Katayama, T. Shimojima, H. Murakawa, Y. Kaneko, W. Malaeb, S. Shin, K. Ono, H. Kumigashira, R. Arita, N. Nagaosa, H. Y. Hwang, Y. Tokura and K. Ishizaka, *Phys. Rev. Lett.*, 2013, **110**, 107204.
42 Q. Liu, Y. Guo and A. J. Freeman, *Nano Lett.*, 2013, **13**, 5264–5270.
43 Q. Zhang and U. Schwingenschlögl, *Phys. Rev. B*, 2018, **97**, 155415.
44 A. J. Bradley, *Philos. Mag.*, 1924, **48**, 477–496.
45 A. S. Avilov and R. M. Imamov, *Kristallografiya*, 1969, **14**, 330–331.
46 J. Kang, S. Tongay, J. Zhou, J. Li and J. Wu, *Appl. Phys. Lett.*, 2013, **102**, 012111.
47 V. E. Bottom, *J. Appl. Phys.*, 1970, **41**, 3941–3944.
48 I. Vurgaftman and J. R. Meyer, *J. Appl. Phys.*, 2003, **94**, 3675–3696.
49 K. S. Novoselov, A. Mishchenko, A. Carvalho and A. H. Castro Neto, *Science*, 2016, **353**, aac9439.
50 R. Fei, W. Li, J. Li and L. Yang, *Appl. Phys. Lett.*, 2015, **107**, 173104.

 This journal is © the Owner Societies 2019